Scripta Materialia 189 (2020) 140–144

Contents lists available at ScienceDirect

Scripta Materialia

journal homepage: www.elsevier.com/locate/scriptamat

Stiff, strong and ductile heterostructured aluminum composites reinforced with oriented nanoplatelets

Jinfeng Nie[a,*], Yuyao Chen[a], Xiang Chen[a], Xiangfa Liu[b,*], Guiliang Liu[b], Yonghao Zhao[a,*], Yuntian Zhu[c,d]

[a] Nano and Heterogeneous Materials Center, School of Materials Science and Engineering, Nanjing University of Science and Technology, Nanjing 210094, China
[b] Key Laboratory for Liquid-Solid Structural Evolution and Processing of Materials, Ministry of Education, Shandong University, Jinan 250061, China
[c] School of Materials Science and Engineering, Southeast University, Nanjing 211189, China
[d] Department of Materials Science and Engineering, City University of Hong Kong, Hong Kong, China

ARTICLE INFO

Article history:
Received 28 July 2020
Revised 9 August 2020
Accepted 10 August 2020
Available online 22 August 2020

Key words:
Aluminum alloys
Heterogeneous structure
Stiffness
Ductility
Preferential orientation

ABSTRACT

In this study, we report a liquid-solid reaction method combined with preferential particle orientation for fabricating a heterostructured Al_3BC/6061 composite with ultrahigh Young's modulus (105 GPa), high tensile strength (495 MPa) and reasonable ductility (6.2%). The preferential orientation of Al_3BC nanoplatelets contributes to the ultrahigh stiffness, and heterogeneous grain structure of the Al matrix facilitates the development of hetero-deformation induced stress and extra strain hardening, giving rise to high strength and good ductility. These results shed new sights into the untapped potential in improving the mechanical properties of metal matrix composites.

Lightweight aluminum alloys with high strength, ductility and high stiffness are increasingly attractive for applications in automotive, aerospace and biomedical in an effort to improve energy efficiency and reduce emission [1,2]. Unfortunately, such a property profile is hard to be obtained in aluminum and its alloys, as these properties are often mutually exclusive. In particular, the low Young's modulus (stiffness) of Al (70 GPa) is especially hard to improve. Typically, aluminum matrix composites (AMCs) reinforced by high-modulus ceramic particles (e.g. carbides, borides, and nitrides) are conceived to simultaneously elevate their strength and stiffness, but this inevitably leads to low ductility [3–5]. This phenomenon stems from the incompatibility in plastic deformation between the reinforcing particles (hard) and the aluminum matrix (soft), as well as the interfaces where geometrically necessary dislocations (GNDs) and strain gradients are generated. For instance, a 6061 Al matrix composite with a high volume fraction (~25 wt%) of Al_3BC particles exhibits an ultimate tensile strength of ~485 MPa, but comes with severe stress concentration at the particle/Al interfaces and dramatic loss of ductility (less than 2%)[6]. On the other hand, the improvement of stiffness in AMCs was always limited by random orientation of particles and volume fraction limitation due to severe agglomeration [7–11].

In recent years, heterostructured materials have attracted extensive attentions for their superior mechanical properties with diverse microstructures spanning the nanometer to micrometer range [12–15], primarily attributable to the hetero-deformation induced (HDI) strengthening due to the accumulation of geometrically necessary dislocations (GNDs) [16–18]. For instance, soft micro-grained Ti lamellae embedded in hard ultrafine-grained Ti lamella matrix allows for remarkably high strain-hardening rate and consequent high ductility [15]. Inspired by this concept, our previous work has firstly demonstrated that a heterostructured Al-($TiC+TiB_2$) composite containing the bimodal grain structure in the matrix was substantiated to have superior combination of strength and ductility, compared to traditional particles reinforced AMCs with homogenous structure [19]. However, it remains a challenge to further enhance its stiffness largely due to the randomly distributed particles.

Herein, we report a heterostructured Al_3BC_p/6061 composite with ultrahigh stiffness (comparable to that of titanium alloys [20]), high ultimate tensile strength and good ductility, a combination superior to that of nearly all reported AMCs [21–27]. Our novel strategy primarily relies on the combination of the heterogeneous structured Al matrix and the preferential distribution of anisotropic nanoplatelets, in such a way to attain a superior prop-

* Corresponding author.
E-mail addresses: niejinfeng@njust.edu.cn (J. Nie), xfliu@sdu.edu.cn (X. Liu), yhzhao@njust.edu.cn (Y. Zhao).

https://doi.org/10.1016/j.scriptamat.2020.08.017
1359-6462/

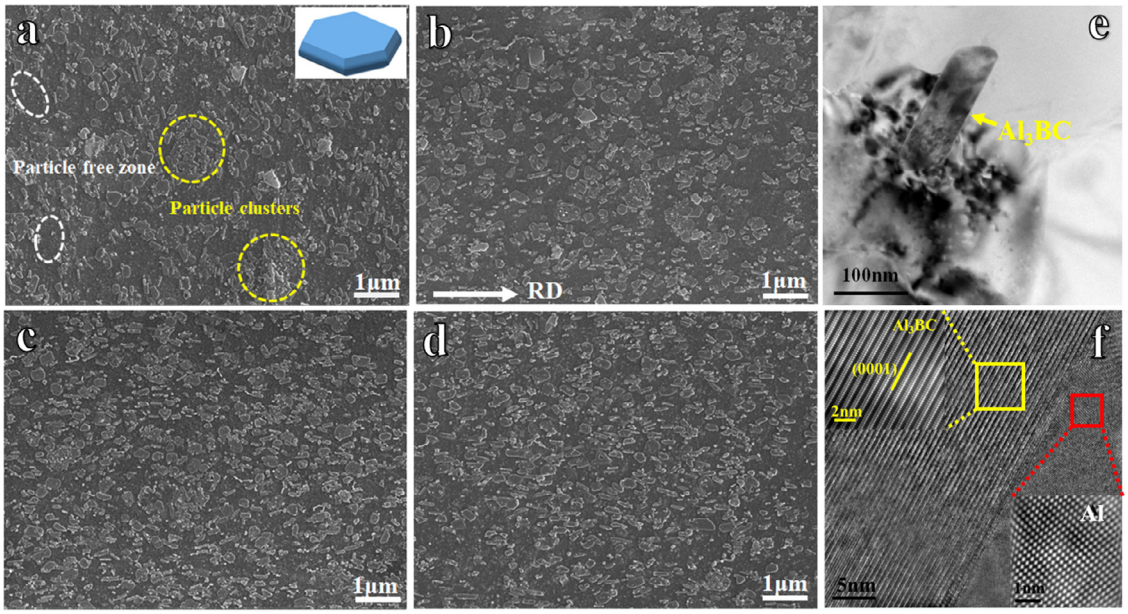

Fig. 1. Microstructures of Al_3BC/6061 composites (RD-ND plane) showing the distribution and orientation of Al_3BC: (a) EXT, morphology of Al_3BC shown in inset of a; (b) HR80; (c) HR90; (d) HR95; (e) An HRTEM image of Al_3BC; (f) A typical lattice fringe image of Al-Al_3BC interface. Insets are the fourier-filtered HRTEM image of the marked red and yellow rectangles are in (f) showing the lattice fringes of Al matrix and Al3BC; Inset of (e) shows the corresponding fast Fourier transformation (FFT) of (f) indicating the crystal orientation relationship of Al_3BC and α-Al. (For interpretation of the references to color in this figure legend, the reader is referred to the web version of this article.)

erty profile. Furthermore, the underpinning mechanisms will be critically appraised by HDI stress measurements and stiffness analysis.

Commercial Al powders (99.7%, mean particle size ~50 μm), boride plasmid powders (99.5%, mean particle size ~2 μm), commercial pure Si powders (99.7%) and commercial pure Mg powders (99.7%) were used to fabricate Al_3BC_p/6061 nanocomposite by a liquid-solid reaction method combined with subsequent hot extrusion process with a ratio of approx. 30 at 500 °C, as reported in our previous work [6]. Furthermore, the extruded composites (referred as EXT sample) were subjected to hot rolling with a reduction of about 80%, 90% and 95% to orient the distribution of Al_3BC nanoplatelets, which is referred to as particle orienting treatment. The above samples are referred to as HR80, HR90 and HR95, respectively. Prior to each rolling pass, the sample was preheated at 500 °C for 30 min in the furnace.

The tensile specimens were machined from the processed sheets with a gauge size of 10 × 2.5 × 1 mm^3 oriented along the rolling direction (RD). Then the tensile samples were tested at room temperature with a universal tensile testing machine (LFM-20, $W+B$) at an initial strain rate of 3 × 10^{-3} s^{-1} (quasi-static). The tensile tests were repeated three times for each specimen. The microstructures were characterized on the RD-ND plane of the sheets using a field emission scanning electron microscope (FESEM, Quanta 250F). A Titan G2 transmission electron microscope (TEM) with a spherical aberration image corrector operated at 300 kV was used to characterize the phase interface. High-angle annular dark-field (HAADF) scanning transmission electron microscopy (STEM) operated at 300 kV was employed to examine the interface structure. TEM foils were prepared with mechanical polishing to the thickness of approx. 25 μm and then thinned by ion beam using Gatan 691 precision ion polishing system.

Fig. 1a shows the microstructure of the EXT sample and Al_3BC particle exhibits the hexagonal platelet morphology (inset of Fig. 1a). The mean size of the platelet is about 245 nm in length and 75 nm in height with an aspect ratio of ~3.3, according to our previous investigation [6]. In the EXT sample, particle-rich zones and particle-free zones are discernable, due to serious agglomeration of Al_3BC particles. While for the HR80, HR90 and HR95 samples, the particle clusters are dispersed and Al_3BC particles tend to be uniformly distributed after the thermo-mechanical treatment (Fig. 1b–d). The hexagonal particles are susceptible to be alignment in the direction of the least resistance during deformation, and show a distinct preferred orientation, i.e. $\{0001\}_{Al3BC}$//RD. The interface structure of Al_3BC particles and the matrix were further investigated by HRTEM characterization and lattice fringe images of a single Al_3BC and Al matrix are shown in Fig. 1e and f. The Al_3BC particles orient to the $[10\bar{1}0]$ direction, and the α-Al matrix orients to the $[\bar{1}22]$ direction as shown in the inset of Fig. 1e, respectively. From the lattice fringe image (see Fig. 1f), the interface is semi-coherently bonded and the (0001) plane of Al_3BC is parallel to the $(01\bar{1})$ plane of α-Al. The robust atomic bonding between Al_3BC and the matrix will play an utmost role in the inherent strength enhancement. In addition, the Al matrix shows a heterogeneous grained structure constituted by two domains of elongated coarse grains and exquiaxed fine-scale grains, which evolve with the deformation process (see Fig. S1).

Table 1
Tensile properties and stiffness of the Al_3BC/6061 composites.

Samples	YS/MPa	UTS/MPa	UE/%	EI/%	E/GPa
EXT	328±4	447±4	4.5±0.5	4.8±0.5	72.9±2.4
HR80	356±4	463±3	4.9±0.3	5.4±0.3	80.9±2.6
HR90	358±3	495±4	5.3±0.3	6.2±0.3	105.0±2.8
HR95	517±5	577±6	1.5±0.1	1.7±0.1	108.6±1.6

The yield strength (YS) and ultimate tensile strength (UTS) of the EXT sample are measured to be ~328 MPa and ~447 MPa, with a corresponding uniform elongation (UE) of ~4.5% (Table 1). From tensile engineering stress–strain curves of the composites with different strains (Fig. 2a), one may see that the YS, UTS and UE for the HR80 and HR90 samples increase simultaneously with increas-

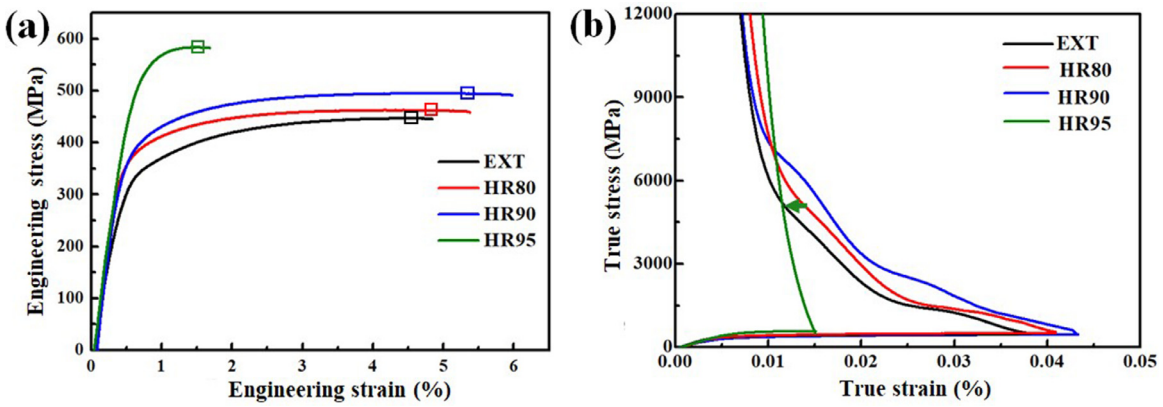

Fig. 2. Tensile properties of the Al_3BC/6061 composites: (a) engineering tensile stress–strain curves; (b) strain hardening rate curves.

ing deformation strain. It is also noticed that the elastic modulus (E) determined from the tensile tests increases from 72.9 GPa for the EXT sample to 105 GPa for the HR90 sample. To our knowledge, such a superior combination of strength-ductility-stiffness in the Al-based composite has not been reported before [18]. With a further increase of the rolling reduction to 95%, both YS and UTS of the HR95 sample increase substantially to 517 MPa and 577 MPa, pointing to a ~57.6% and 29.1% increment compared to the as-received one. The E of the HR95 composite reaches a maximum value of 108.6 GPa, 35.7 GPa higher than that of the EXT sample. However, the UE of the HR95 sample drops drastically to 1.7%.

It is known that the onset of localized deformation, e.g. necking instability, occurs due to the low work hardening behavior of a material, according to Hart criterion [28,29] described as:

$$\frac{d\sigma}{d\varepsilon} \leq (1-m)\sigma$$

where σ is the true stress, ε is the true strain and m is the strain rate sensitivity. For ultra-fine grained and nanostructured metals, m is not sufficiently high (<0.05) at room temperature and is thus neglected [30,31]. The work-hardening rate ($\Theta = d\sigma/d\varepsilon$) curve of the EXT sample decreases rapidly with increasing strain (Fig. 2b). In contrast, both the HR80 and HR90 samples display a slower Θ decrease. Θ values of the HR80 and HR90 samples are larger than that of the EXT sample, suggesting a better Θ-retention and an improved strain hardening. Besides, Θ value of HR90 is higher than that of HR80, pointing to the enhanced ductility. However, the Θ value of HR95 sample decreases faster than the EXT sample and is much lower than that of EXT when the true strain is larger than a critical value of 1.15% as indicated by the green arrow in Fig. 2b. Hence, the reduced strain hardening rate leads to the low ductility of HR95 sample.

In order to quantify the HDI effect from the heterostructure, the HDI stress was measured according to the loading-unloading-reloading tensile curves, see Fig. S2(a and b). Each curve exhibits a hysteresis loop. For the Al_3BC/6061 nanocomposites, the calculated HDI stress contributes over 50% (~230 MPa) to the flow strength as seen in Fig. S2(c and d). Strain hardening primarily derives from the dislocation accumulation ability of the softer grains. Upon tensile straining, large strain gradients near the interfaces between small and large grains (Fig. S1) are produced during deformation, which enables a significant HDI stress to strengthen the material and high HDI work hardening for good ductility [13]. By contrast, the dislocation accumulation ability is reduced due to the uniform ultrafine grains in the HR95 sample (Fig. S1d), as manifested by the typical monotonic drop in Θ (Fig. 2b). It is reasonable to believe that the increased HDI stress caused by the pilling up of geometrically necessary dislocations (GNDs) for the heterostructured HR80 and HR90 samples is the main reason for the enhanced strain hardening ability. However, it is noticed that both the volume fraction and the grains sizes of the elongated coarse grains (ECG) in these two sample are reduced (Fig. S1g and h), in which more dislocations can be stored in theory. Actually, the HDI hardening in heterostructured materials is mainly influenced related to the strain gradient in the interface affected zones (IAZs) [32]. There is a critical IAZ width in heterogeneous lamella structures materials that is not affected by the layer thick until adjacent IAZs start to overlap [32,33]. Therefore, it indicates that the IAZ width will not be influenced by the reduced width and volume fraction of ECG domains. However, the strain gradient in the IAZ increases with increasing tensile strain, which indicates the enhanced GNDs density both in the HR80 and HR90 samples leads to the higher work hardening rate.

To further account for the contribution of Al_3BC particles to the high stiffness, Al_3BC particle's orientation evolution with respect to RD and its relationship with the E were investigated. Herein, the θ angle of {0001} planes of an Al_3BC platelet with respect to RD was used to describe the particle's orientation and at least one hundred particles were counted to determine the average orientation angle θ. The statistics in Fig. 3a shows the average angle decreases gradually from 62° to 9 °, indicating that most particles with {0001} orientation are parallel to RD. Furthermore, variation of the composites' E with the platelets' orientation shows that the E increases linearly with a decrease of θ value (Fig. 3b). In addition, the composites' E value was measured with changing the angle α, a parameter between the tensile direction and the preferred orientation (RD) (see Fig. 3c inset). As expected, the E value of HR95 decreases from 108.6 GPa to 83.3 GPa and 72.1 GPa with an increase of α from 0° to 45° and 90°. While for the HR80 sample, the E values slightly change without pronounced anisotropy.

Our work has demonstrated that the Young's modulus of metals can be considerably elevated by in-situ formation of stiff nanoplatelets and then mechanically orientating them to the loading direction. Several research groups have developed high modulus composites through in-situ formation of high modulus phases [34,35], by manipulating the particle size, distribution and the interface structure [36–38]. For instance, Ji et al. have utilized stiff TiB_2 nano particles (E ~565 GPa) to enhance E of Al-Si-Mg alloy up to ~94 GPa [21]. Here by orienting of anisotropic nanoplatelets, the E of the Al_3BC/Al composites (HR95 sample) reaches an ultra-high value of ~108.6 GPa, much higher than that of the 6061Al (~70 GPa) and even comparable to that of Ti-6Al-4V (105–116 GPa) [20]. It was revealed that the Halpin-Tsai model can be used to predict the Young's modulus of composites sophistically by con-

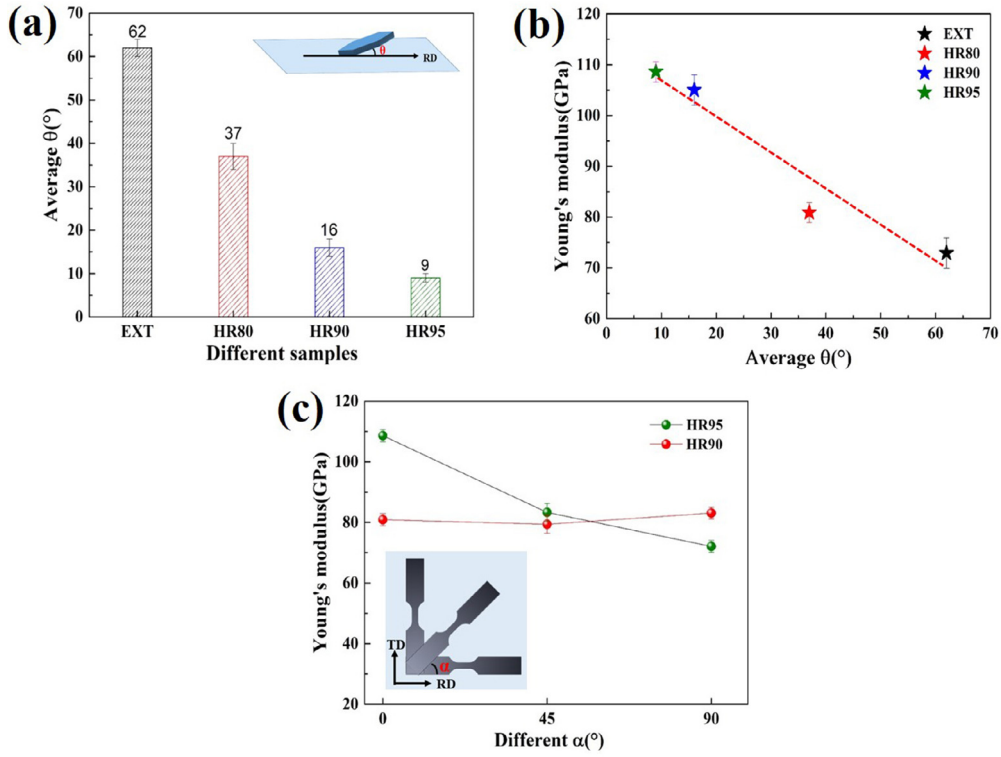

Fig. 3. The relationship of Al_3BC platelets' orientation and the composites' *E* values: (a) variation of average orientation angle (θ) of Al_3BC platelets; (b, c) variations of the E with the platelets' orientation (θ) and the tensile direction (α) with respect to RD, respectively.

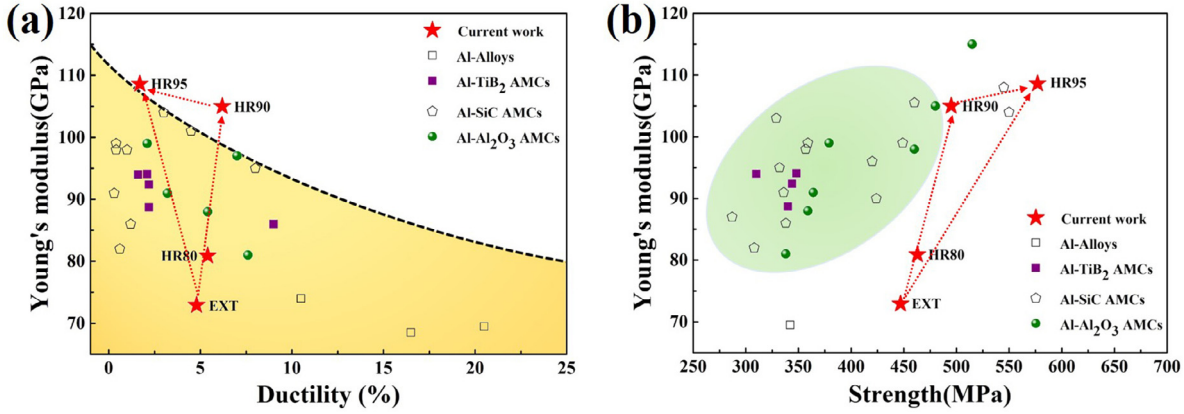

Fig. 4. The Young's modulus versus ductility (a) and the versus with tensile strength (b) for current Al_3BC/6061 composites. Other data of AMCs were shown for comparison.

sidering the aspect ratio of reinforcement particles [39], i.e.

$$E = E_M\left(\frac{1+2\xi\eta V_P}{1-\eta V_P}\right) \quad (1)$$

$$\eta = \left(\frac{E_P}{E_M}-1\right)\Big/\left(\frac{E_P}{E_M}+2\xi\right) \quad (2)$$

where E_P and E_M are the Young's modulus of the particles and the matrix, respectively. V_P is the volume fraction of particle, ξ is the aspect ratio of the particulate reinforcement. As such, using the parameters for Al_3BC (E_x = 326 GPa, E_z = 294 GPa [40], V_p = 24.1%, and ξ = 3.3), the E of HR95 is estimated to be approximately in the range of 110–115 GPa, which is in good agreement with the experimentally determined value for the HR95 sample. This analysis supports the efficiency and effectiveness in improving the stiffness in our novel method. The main issue we can expect is how to further control the orientation of anisotropic particles.

Plotting E vs. ductility and E vs. strength for the Al_3BC/Al nanocomposites in the present study and other reported AMCs [22–27], one may find that both modulus-ductility and modulus-strength synergy of Al_3BC/Al are distinct from most reported AMCs. The highest E value of Al_3BC/Al nanocomposite is ~55% higher than that of the current aluminum alloys [7]. Imperatively, the ductility of the HR90 sample is almost twice as high as that of reported Al-SiC AMCs at the same E level (Fig. 4a). The remarkable stiffness improvement for the HR90 sample is achieved without the sacrifice of ductility. In addition, the E seemingly elevates with the increase of strength for most AMCs, see Fig. 4b. The strength-modulus synergy in the HR90 and HR95 samples is also obviously better than the reported data of the conventional AMCs.

In summary, we successfully achieved a superior stiffness-strength-ductility property profile in an intentionally designed Al_3BC/6061 matrix composite. The orienting of anisotropic Al_3BC nanoplatelets gives rise to high stiffness and the heterogeneous grain structure of aluminum matrix brings about additional HDI hardening with deformation leading to high strain hardening rate. Generally, the liquid-solid reaction method combined with traditional extrusion or rolling processes can be readily scaled for industrial production. We are now focused on extending the concepts demonstrated here to other lightweight metal combinations (Table 1).

Declaration of Competing Interest

The authors declare that they have no known competing financial interests or personal relationships that could have appeared to influence the work reported in this paper.

Acknowledgements

This work is supported by the National Key R and D Program of China (No. 2017YFA0204403), Key Program of National Natural Science Foundation of China (Nos. 51731007 and 51931003), the National Natural Science Foundation of China (Nos. 51971112 and 51501092), the Fundamental Research Funds for the Central Universities (Nos. 30920021160 and 30919011405). The authors also want to acknowledge the support of the Jiangsu Key Laboratory of Advanced Micro-Nano Materials and Technology. SEM, TEM and EBSD experiments are performed at the Materials Characterization and Research Center of Nanjing University of Science and Technology.

Supplementary materials

Supplementary material associated with this article can be found, in the online version, at doi:10.1016/j.scriptamat.2020.08.017.

References

[1] P.V. Liddicoat, X.Z. Liao, Y.H. Zhao, Y.T. Zhu, M.Y. Murashkin, E.J. Lavernia, R.Z. Valiev, S.P. Ringer, Nat. Commun. 1 (2010) 1–7.
[2] Z. Wang, R.T. Qu, S. Scudino, B.A. Sun, K.G. Prashanth, J. Eckert, NPG Asia Mater. 7 (2015) 1–8.
[3] Y.F. Liu, F. Wang, Y. Cao, J.F. Nie, H. Zhou, H.B. Yang, X.F. Liu, X.H. An, X.Z. Liao, Y.H. Zhao, Y.T. Zhu, Scr. Mater. 162 (2019) 316–320.
[4] J.F. Nie, F.H. Lu, Z.W. Huang, X. Ma, H. Zhou, C. Chen, X. Chen, H.B. Yang, Y. Cao, X.F. Liu, Y.H. Zhao, Y.T. Zhu, Material 9 (2020) 100523.
[5] Q.L. Zhao, H.D. Zhang, X.X. Zhang, Q. Feng, Q.C. Jiang, Mater. Sci. Eng. A 718 (2018) 305–310.
[6] Y.F. Zhao, Z. Qian, X.F. Liu, Mater. Des. 93 (2016) 283–290.
[7] A.W. Zhu, A. Csontos, E.A. Starke, Acta Mater. 47 (1999) 1713–1721.
[8] L.Y. Chen, J.Q. Xu, H. Choi, M. Pozuelo, X.L. Ma, S. Bhowmick, J.M. Yang, S. Mathaudhu, X.C. Li, Nature 528 (2015) 539–543.
[9] N. Ramakrishnan, Acta Mater. 44 (1996) 69–77.
[10] A. Mortensen, J. Llorca, Annu. Rev. Mater. Res. 40 (2010) 243–270.
[11] J.C. Li, X.X. Zhang, L. Geng, Mater. Des. 144 (2018) 159–168.
[12] Y.T. Zhu, X.L. Wu, Mater. Res. Lett. 7 (2019) 393–398.
[13] Y.T. Zhu, X.L. Wu, Mater. Res. Lett. 5 (2017) 527–532.
[14] G. Wu, C. Liu, L.G. Sun, Q. Wang, B.A. Sun, B. Han, J.J. Kai, J.H. Lian, C.T. Liu, K. Cao, Y. Lu, L.Z. Cheng, J. Lu, Nat. Commun. 10 (2019) 5099.
[15] X.L. Wu, M.X. Yang, F.P. Yuan, G.L. Wu, Y.J. Wei, X.X. Huang, Y.T. Zhu, Proc. Natl. Acad. Sci. USA 112 (2015) 14501–14505.
[16] J. Llorca, A. Needleman, S. Suresh, Scr. Metall. Mater. 24 (7) (1990) 1203–1208.
[17] C.W. Sinclair, G. Saada, J.D. Embury, Philos. Mag. 86 (25–26) (2006) 4081–4098.
[18] L. Thilly, S. Van Petegem, P.O. Renault, F Lecouturier, V. Vidal, B. Schmitt, H. Van Swygenhoven, Acta Mater. 57 (11) (2009) 3157–3169.
[19] Y.Y. Chen, J.F. Nie, F. Wang, H.B. Yang, C.C. Wu, X.F. Liu, Y.H. Zhao, J. Alloy. Compd. 815 (2020) 152285.
[20] Q.Z. Li, E.Y. Chen, D.R. Bice, D.C. Dunand, Metall. Mater. Trans. A 39 (2008) 441–449.
[21] S.X. Ji, F. Amirkhanlu, A. Mostaed, R. Beanland, Mater. Sci. Eng. A 763 (2019) 138072.
[22] I. Ibrahim, F. Mohamed, E. Lavernia, J. Mater. Sci. 26 (1991) 1137–1156.
[23] S. Amirkhanlou, R. Jamaati, B. Niroumand, M.R. Toroghinejad, J. Mater, Process. Technol. 211 (2011) 1159–1165.
[24] Z. Fan, Y. Wang, Y. Zhang, T. Qin, X.R. Zhou, G.E. Thompson, T. Pennycook, T. Hashimoto, Acta Mater. 84 (2015) 292–304.
[25] Y.N. Zan, Y.T. Zhou, Z.Y. Liu, G.N. Ma, D. Wang, Q.Z. Wang, W.G. Wang, B.L. Xiao, Z.Y. Ma, Mater. Des. 166 (2019) 107629.
[26] Q. Zheng, R.G. Reddy, Metall. Mater. Trans. B 34 (6) (2003) 793–804.
[27] A. Kumar, P. Jha, M. Mahapatra, J. Mater, Eng. Perform. 23 (3) (2014) 743–752.
[28] J.W. Hutchinson, K.W. Neale, Acta Metall. 25 (1977) 839–846.
[29] Y.T.X.L.Wu Zhu, Mater. Today Nano 2 (2018) 15–20.
[30] M. Dao, L. Lu, Y.F. Shen, S. Suresh, Acta Mater. 54 (2006) 5421–5432.
[31] M.D. Gram, J.S. Carpenter, P.M. Anderson, Acta Mater. 92 (2015) 255.
[32] H.W. Höppel, C.X. Huang, Y.F. Wang, X.L. Ma, S. Yin, M. Göken, X.L. Wu, H.J. Gao, Y.T. Zhu, Mater. Today 21 (2018) 713–719.
[33] J. Moering, X.L. Ma, C.X. Huang, M. Ruppert, H.W. Höppel, M. Göken, J. Narayan, Y.T. Zhu, Acta Mater. 116 (2016) 43–52.
[34] A. Szczepaniak, H. Springer, R. Aparicio-Fernández, C. Baron, D. Raabe, Mater. Des. 124 (2017) 183–193.
[35] C. Baron, H. Springer, D. Raabe, Mater. Des. 111 (2016) 185–191.
[36] H. Springer, R.A. Fernandez, M.J. Duarte, A. Kostka, D. Raabe, Acta Mater. 96 (2015) 47–56.
[37] S. Lartigue-Korinek, M. Walls, N. Haneche, L. Cha, L. Mazerolles, F. Bonnet, Acta Mater. 98 (2015) 297–305.
[38] Z. Hadjem-Hamouche, J.P. Chevalier, Y. Cui, F. Bonnet, Steel Res. Int. 83 (2012) 538–545.
[39] M. Wang, D. Chen, Z. Chen, Y. Wu, F. Wang, N. Ma, H. Wang, Mater. Sci. Eng. A 590 (2014) 246–254.
[40] J.Y. Wang, Y.C. Zhou, T. Liao, Z.J. Lin, Appl. Phys. Lett. 89 (2006) 021917.